IEEE Access
Multidisciplinary | Rapid Review | Open Access Journal

Received December 6, 2021, accepted December 13, 2021, date of publication December 16, 2021,
date of current version January 5, 2022.

*Digital Object Identifier 10.1109/ACCESS.2021.3136255*

# Feasibility of a 64-Channel Scintillation Fiber System for Real-Time Monitoring of Dwell Positions and Dwell Times of High-Dose-Rate Brachytherapy Sources

**NA HYE KWON[1], JINSUNG KIM[1,2], JU HYE KIM[3], SANG HYOUN CHOI[4], AND DONG WOOK KIM[1,2], (Member, IEEE)**

[1]Department of Radiation Oncology, Yonsei University College of Medicine, Yonsei University, Seoul 03722, South Korea
[2]Department of Radiation Oncology, Yonsei Cancer Center, Yonsei University College of Medicine, Seoul 03722, South Korea
[3]Department of Radiation Oncology, Samsung Medical Center, Seoul 06351, South Korea
[4]Department of Radiological Physics and Engineering, Korea Institute of Radiological and Medical Sciences, Seoul 01812, South Korea

Corresponding authors: Sang Hyoun Choi (shchoi@kirams.re.kr) and Dong Wook Kim (joocheck@gmail.com)

This work was supported in part by the Nuclear Safety Research Program through the Korea Foundation of Nuclear Safety (KoFONS) using Financial Resources granted by the Nuclear Safety and Security Commission (NSSC) of the Republic of Korea under Grant 2003013, and in part by the National Research Foundation of Korea (NRF) funded by the Korean Government under Grant 2020M2D9A3094170 and Grant 2018R1D1A1B07050217.

**ABSTRACT** A 64-channel scintillation fiber-based real-time monitoring system (SFRMS) was developed and evaluated to verify the dwell position and dwell time of the radioactive source in high-dose-rate brachytherapy. The measurement system consists of 64 sensors installed around a tandem applicator. The distal end of the readout system was fiber-optically connected to the measurement system. The data readout system consisted of a photomultiplier tube and a measurement and automation explorer. The SFRMS accuracy was evaluated in terms of dwell position, output linearity, and dwell time using an afterloader with a $^{192}$Ir source. Additionally, a Gafchromic EBT3 film was inserted into the applicator to compare fiber measurements. Furthermore, a clinical treatment plan and silicon-based anthropomorphic phantom were utilized to evaluate the accuracy of the dwell positions and dwell times of the source in a situation mimicking a real treatment. The measured output signals from each sensor were fit with Gaussian and inverse-square functions to determine the exact source dwell positions. The difference in dwell position between the plans and the estimated data was $-0.63 \pm 0.25$ mm for the Gaussian fitting and $0.72 \pm 0.26$ mm for the inverse-square fitting. The difference in dwell time between the plans and the estimated data was within 0.1 sec. For the measurements of the clinical plan on the silicon-based anthropomorphic phantom, the difference in dwell position between the plans and the estimated data was less than $0.88 \pm 0.29$ mm for the Gaussian fitting and less than $0.85 \pm 0.36$ mm for the inverse-square fitting. The SFRMS can accurately detect source dwell positions and dwell times and provide real-time output.

**INDEX TERMS** Index terms dwell position, dwell time, high-dose-rate brachytherapy, real-time monitoring, scintillation fiber.

## I. INTRODUCTION

High-dose-rate (HDR) brachytherapy (BT) is a radiotherapy technique used to treat cancer that uses sealed radioactive sources to deliver doses at a rate greater than 12 Gy/h [1], [2]. The radioactive source in HDR-BT travels through tubes or applicators, providing a highly conformal dose escalation to cancer areas. HDR-BT is used to treat cancers of the prostate, rectum, cervix, esophagus, and other organs [3], [4]. For cervical, prostate, or gynecologic cancers, HDR-BT is more effective than external beam radiation therapy at targeting cancerous tissues while protecting surrounding normal tissues [4]–[7]. However, to utilize these advantages effectively, it is necessary to ensure the accuracy of the dwell positions and dwell times of the BT sources [8], [9].

In BT, quality assurance (QA) must be performed on treatment equipment, treatment planning systems, and patient treatment procedures. Specifically, the accuracy of loading

The associate editor coordinating the review of this manuscript and approving it for publication was Marco Giannelli.

and positioning the source and dummy should be checked on a weekly or monthly basis. Furthermore, the accuracy of the irradiation time should be checked quarterly or whenever the source changes. Quality verification definitions and specifications can be found in the IAEA Technical Documents (IAEA-TECDOC) 1040 and the report of Task Group 59 of the American Association of Physicists in Medicine (AAPM) [10], [11].

Recently, various types of equipment have been introduced to external beam radiation therapy (EBRT) for real-time patient monitoring during treatment, including Dolphin (IBA Dosimetry, Schwarzenbruck, Germany), IQM (iRT Systems GmbH, Koblenz, Germany), and PerFraction (Sun Nuclear Corporation, Melbourne, FL, USA) [12]–[14]. In contrast to the EBRT, however, the lack of proper monitoring in BT treatment has gained attention over the last decade.

BT dose evaluation has been investigated in several studies. Smith *et al.* [15] evaluated EPID-based in vitro dosimetry for BT and reported the effects of source-to-detector distances. They reported that there is uncertainty due to the low transmission doses caused by the lower energy of BT.

Jeang *et al.* [16] described an alternative method for 2-dimensional in vivo rectal dosimetry for HDR-BT for cervical cancer using an endorectal balloon (ERB) with a Gafchromic EBT3 film (Ashland ISP Advanced Materials, NJ, USA). They showed that ERBs can be used for HDR-BT to monitor the accuracy and consistency of cervical and prostate cancer treatments, as well as to predict rectal toxicity. EBT3 films are widely used for dose evaluation because they can measure doses independently of HDR-BT systems. However, when using these conventional film-reading techniques, the dose effects can only be evaluated after film exposure [17]. Furthermore, EBT3 films require a waiting period of a few hours before the values can be obtained; hence, real-time monitoring is limited.

In 2007, Qi *et al.* [18] presented a phantom verification method for an HDR-BT plan based on the use of a MOSFET detector. They reported the mean relative deviation between the treatment plan and the measurement to be $2.2 \pm 0.2\%$ for dose points 1 cm away from the source and $2.0 \pm 0.1\%$ for dose points 2 cm away from the source. Point doses were evaluated in the study, but the dwell time and dwell position of the source were not considered.

Proulx *et al.* [19] evaluated the accuracy of a plastic scintillation detector (PSD) system for in-phantom dosimetry during $^{192}$Ir HDR-BT treatments. They reported that a PSD can perform accurate dosimetry. The authors showed the applicability of PSDs for in vivo dosimetry (IVD) for HDR-BT. Recently, Debnath *et al.* [20] reported on the performance of a real-time dose verification system for BT developed using a point size inorganic scintillator detector. They reported that the standard deviation ($1\sigma$) of the signal magnitudes provided by their system was 0.03%, and that the stability was within 0.54%. Kertzscher *et al.* [21] reported the measurement results for 20 treatments in 12 prostate cases, demonstrating the potential of time-resolved IVD using radioluminescence signals from Al2O3:C crystals. Recently, his group reported the accuracy of an IVD-based source-tracking method with a comparable system to HDR-BT [20], [22]. They reported an accuracy range of $-0.01 \pm 0.38$ to $2.8 \pm 0.38$ mm. However, to achieve precise dwell position monitoring with the PSD system in a clinical setting, factors such as detector sensitivity, catheter positioning accuracy for the PSD, and medium uniformity should be considered.

Mason *et al.* [23] performed Monte Carlo simulations of a single-fraction treatment to compare data measured with a MOSFET inserted into a needle. The point dose was evaluated in their investigation, but the source movement and irradiation time were not.

Kertzscher *et al.* reported on IVD trends and prospects for BT in 2014 [24], noting that multipoint dosimeters, such as linear-array MOSFETs and plastic scintillator detectors, would become novel dosimeter IVD detectors for BT. In 2020, Verhaegen *et al.* suggested that IVD approaches provide benefits only if the techniques are commercially available, straightforward to implement in clinical practice, require minimal and easy-to-perform QA procedures, and are accurate enough to detect the relevant error [25]. Additionally, in 2020, Fonseca *et al.* reported on the requirements and future directions of IVD in BT [26]. They reviewed the results of previous studies and noted that more than 10% of dose errors could have severe clinical effects. They introduced two recent IVD methods: time-integrated point/multipoint dosimetry and time-resolved point/multipoint dosimetry. They stated that time-resolved methods could avoid large treatment errors, which are impossible with time-integrated dosimetry.

In this study, we developed a scintillation fiber-based real-time monitoring system (SFRMS) for HDR-BT and evaluated its performance by measuring dwell positions and dwell times. Moreover, we implemented a real patient plan using an in-house silicon phantom developed based on general human anatomy, including the pelvis, bladder, vagina, rectum, and anus. Then, the applicability of the SFRMS to the patient treatment plan was evaluated.

## II. MATERIALS AND METHODS

### A. SYSTEM LAYOUT

#### 1) SCINTILLATION AND OPTICAL FIBERS

We developed a tandem applicator measurement system for HDR-BT (i.e., the SFRMS) that consists of 64-channel plastic scintillation fibers. We used a BCF-12 scintillating fiber for signal generation and a BCF-98 optical fiber for signal transmission (Saint-Gobain S.A., France). The BCF-12 and BCF-98 fibers were connected using optical grease (Saint-Gobain's BC-630 optical grease, Saint-Gobain S.A., France) [27]. Both the BCF-12 and BCF-98 fibers are polystyrene-based plastic fibers with square cross-sections (1 mm$^2$), and both scintillation fibers have a cladding thickness of 0.04 mm and a coating thickness of 0.010–0.015 mm;

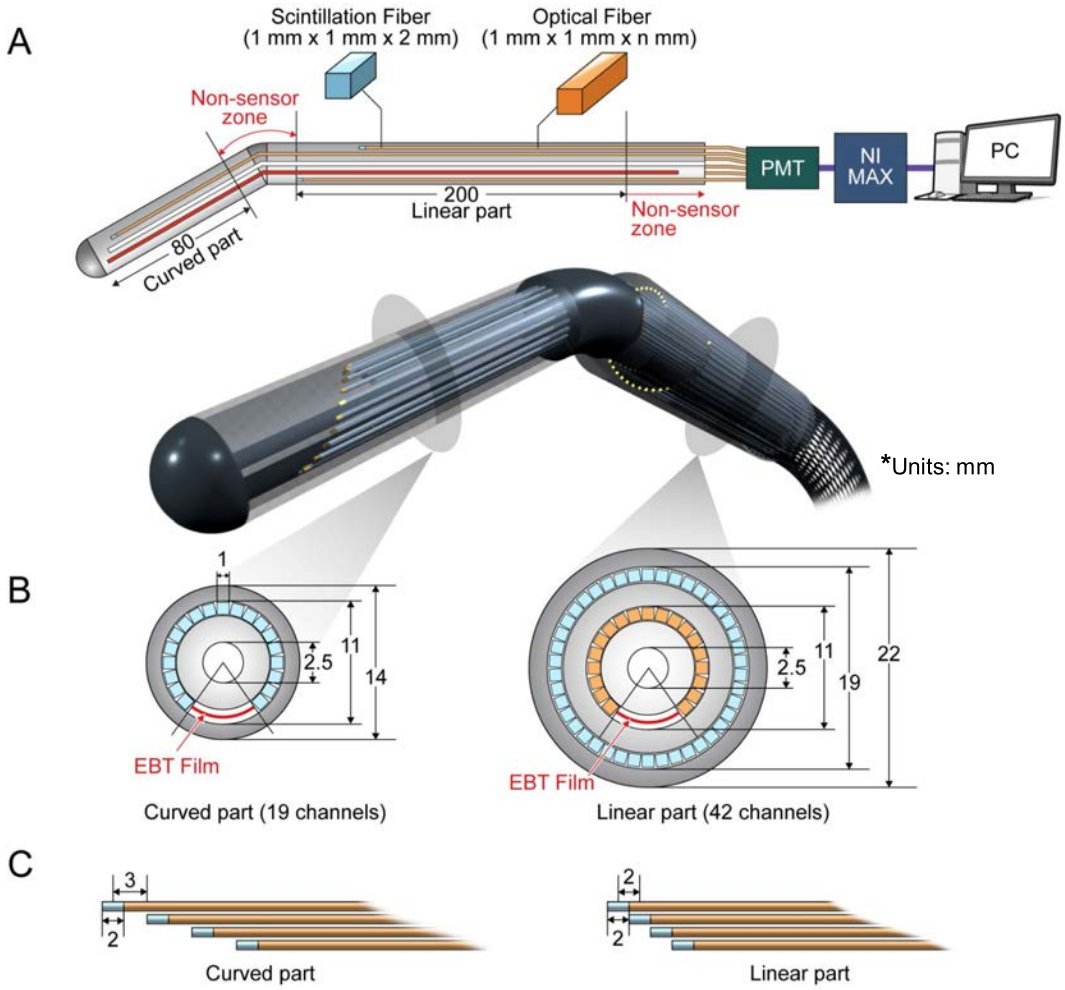


**FIGURE 1.** Diagram of scintillation fiber-based 64-channel applicator: A. Side view of applicator, B. Types of arrangement of curved and straight parts of scintillation fibers and optical fibers, C. Cross sectional view of curved and straight parts of the applicator. (All units are shown in mm).

the black EMA (Extra Mural Absorber) coating applied to the outer fiber surface primarily eliminates fiber crosstalk. The BCF-98 fiber transmits the blue scintillating light generated by the BCF-12 fiber to a photomultiplier tube (PMT, Hamamatsu PMT Assembly, H12428-203 MOD). The BCF-12 fiber has a scintillating light emission peak at 435 nm and a decay time of 3.2 ns [28]. The BCF-98 fiber has a transmission loss of 3.3 dB/m [29].

### 2) APPLICATOR FABRICATION

The homemade 64-channel tandem applicator consisted of a scintillation fiber wrapped around the tube through which the radioactive source moved, as shown in Figs. 1 and 2.

The scintillation fiber (BCF-12) and optical fiber (BCF-98) were 1-mm thick and had square cross-sections. The scintillation fibers (BCF-12) were cut into 2-mm segments and connected to one end of a 1-m-long optical fiber (BCF-98) using optical grease. The other end of the optical fiber (BCF-98) was similarly connected to the PMT (Fig. 1 A). The distance between the centers of two adjacent scintillation fibers was 3 mm in the curved part and 2 mm in the linear part (Fig. 1 B). The applicator consisted of three subparts. The first (innermost) part was an inner tube with a diameter of 2.5 mm through which the radiation source moved back and forth. The second part (curve) is a cover that wraps around the front half of the first part (inner tube), where the sensors are inserted. The sensors are arranged in a cylindrical pattern around the inner tube, 5 mm from the center. The third part (linear) is a cover that wraps around the rear half of the first part (inner tube), where the sensors are inserted. The sensors are arranged in a cylindrical pattern around the inner tube, 9 mm from the center. To evaluate the dwell position independently of the scintillator fiber sensor, we created a thin, long space in which the film could be inserted into the applicator (Fig. 1 C). We also developed a rectum tube to evaluate the dose at the rectum.

There were 64 channels in total, including 19 for the curved part (one dummy source + 18 sensors), 42 for the linear part (one dummy source + 41 sensors), and three for the rectum tubes. The homemade scintillation fiber-based

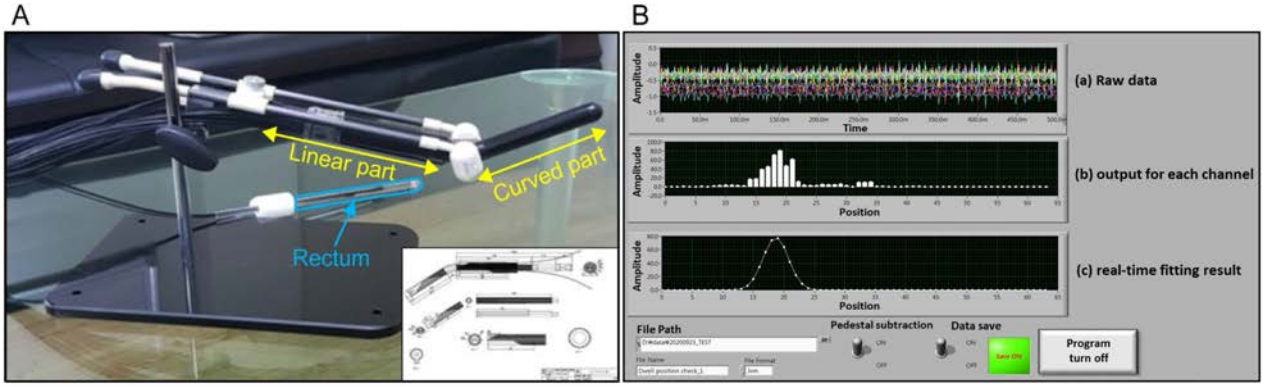


**FIGURE 2.** A. scintillation fiber-based 64-channel applicator, B. graphical user interface (GUI) of the real-time monitoring system : The GUI for the real-time monitoring system consists of three display windows: (a) raw data in real-time, with the horizontal axis representing time, and the vertical axis representing channel-specific output, (b) output for each channel in real-time, with the horizontal axis is the number of each scintillation channel, and the vertical axis representing the output for each channel, and (c) is the real-time fitting results of the data.

64-channel tandem applicator is shown in Fig. 2 A. The applicator consists of a curved part, a linear part, and a tube for the rectum. The holder was designed specifically to secure the applicator.

The primary disadvantage of plastic scintillators is the presence of optical noise, such as Cerenkov radiation and fiber excited luminescence, fluorescence generated in the light guide, which results in an undesirable stem effect [30], [31]. The stem effect is generally referred to as measurement optical noise generated in the optical fiber material. Even when the radiation source approaches the optical fiber rather than the scintillator fiber, the stem effect generates noise. Furthermore, the noise from the stem effect increases as the distance between the source and the optical fiber decreases. In the SFRMS, scintillation fibers (BCF-12) are positioned at 2- or 3-mm intervals at the distal end of the 64 optical fibers (BCF-98), which are arranged at the same distance and are parallel to the source movement line. As the source moves within the applicator, the vertical distance between the source and the optical fibers remains constant. Therefore, the stem effect is generated uniformly across the entire optical fiber and can be separated by total background subtraction. The SFRMS calculates the peak position in the relative output distribution of each sensor. Therefore, the spacing among the arranged sensors is a significant factor in determining position measurement accuracy. In addition, there are two optical fibers that are not connected to the scintillator. The background light is measured and subtracted simultaneously.

#### 3) REAL-TIME DATA READOUT SYSTEM

The overall schematic of the system is shown in Fig. 3. The applicator is connected to the PMT, the DAQ Board, and the NI-DAQmx device in that order. The final signal data are transferred and saved on a computer. To connect the 64 fibers to the PMT, we used a homemade optical connector. As shown in the red box in Fig. 3, we drilled 64 holes in the cube to precisely match each PMT channel.

The real-time measurement screen of the SFRMS is shown in Fig. 2 B, where the signal movement is shown by the dwell position displayed on the screen, alongside the Gaussian fitting applied in real time.

The real-time data readout system was designed using LabVIEW 2012 (National Instruments, Austin, TX, USA) and configured to be controlled by NI-DAQmx software (National Instruments, Austin, TX, USA) on a universal serial-bus-connected laptop for the CompactDAQ system. Fig. 2 B shows the graphical user interface of the real-time data readout system. The user interface displays three windows. In Fig. 2 B, the top window (a) shows the raw data from the system; the middle window (b) shows the data output (vertical) at each channel (horizontal, 64 channels); and the bottom window (c) shows the real-time fitting result for the data shown in the middle window. Raw voltage data (V) were collected every 0.001 s and saved after sampling, amplification, and background processing. The raw data were also saved. The process is described by Eq. (1):

$$DATA_c = \left[\frac{-\int DATA_R}{S}\right] \times A - DATA_b, \tag{1}$$

where $DATA_c$ is the converted data, $DATA_R$ is the raw data, $DATA_b$ is the background data, A is the amplification rate, and S is the sampling size when we obtain the sampled data from the raw data. We used an S of 500 in this study.

### B. ACCURACY VERIFICATION OF THE REAL-TIME MONITORING SYSTEM

We evaluated the accuracy of the SFRMS by measuring the dwell position of the radioactive source sent from the afterloader (microSelectron V3, Elekta Brachytherapy (Nucletron), Veenendaal, Netherland). The minimum source moving step was 2.5 mm, and the total moving range from the tip of the applicator was 4.1–104.1 mm.

In the SFRMS, we collected raw data every 0.001 s (1000 Hz). The operating bias voltage of the PMT was 1300 V. The data were sampled every 0.5 s (500 times).

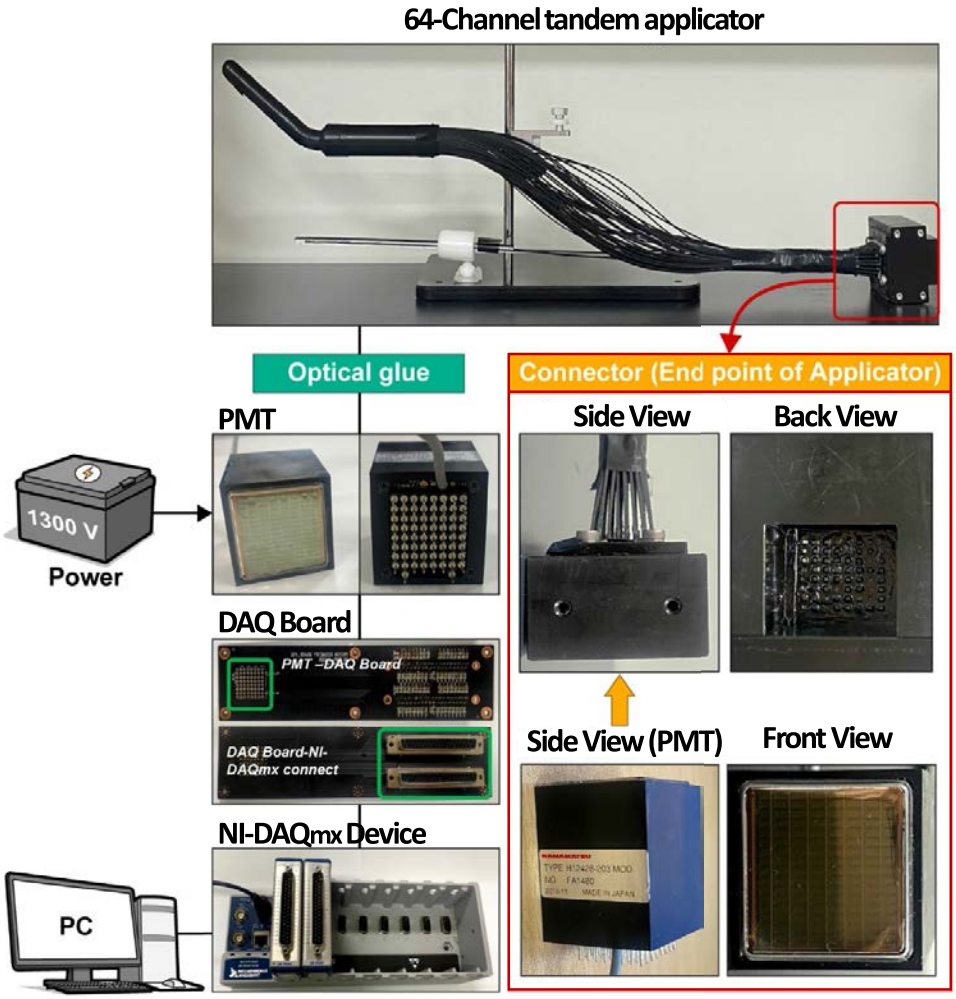


**FIGURE 3.** Overall schematic of the system: The setup of the overall schematic of the system. Applicator is connected to the PMT, the DAQ Board, and the NI-DAQmx device in turn and signal saved at the Computer. An electrometer with a high voltage of 1300 V high voltage is connected to the PMT.

### 1) CHANNEL CALIBRATION COEFFICIENT

We obtained coefficients experimentally to correct for the differences in output and sensitivity for each channel. To determine the calibration coefficient for each channel, the dwell position was set so that the source stopped at 2.5-mm intervals every 10 s, and the response of the proximity sensor at each dwell position was measured.

After the calibration run, the responses of the sensors were normalized based on the inverse-square law for the 3-dimensional distance between the sensor and the source position. The response of the sensor increased as the source moved closer to the sensor and decreased as the source moved further away. We obtained the calibration coefficient, which was the output of each sensor that needed to be calibrated, in order to provide the same maximum power when the source was closest to the sensor.

### 2) DWELL POSITION ACCURACY MEASUREMENT

To test the accuracy of the dwell position, the source was moved in 2.5-, 5.0-, and 10-mm increments from the end of the catheter to the tip. Each measurement was recorded three times.

As shown in Fig. 4, the SFRMS found the dwell position to calculate the peak position, y, using peak positions from the output signals of each sensor. The SFRMS, which performed output calibration on each sensor, found the dwell position by calculating the peak position based on the output signal distribution of each sensor (position).

After calibration, we fitted the data with Gaussian and inverse-square functions to compare the calculated position to the planned source position. We used LabVIEW (National Instruments, Austin, Texas, USA) for Gaussian fitting and Microsoft Excel for inverse-square fitting.

The source position was identified using the Gaussian function by locating the peak position in a 2-dimensional histogram, with the horizontal axis representing the sensor position and the vertical axis representing the real-time output value of the sensor. We compared the planned source position to the fitted data and evaluated the error in terms of the average and standard deviation of the position difference.

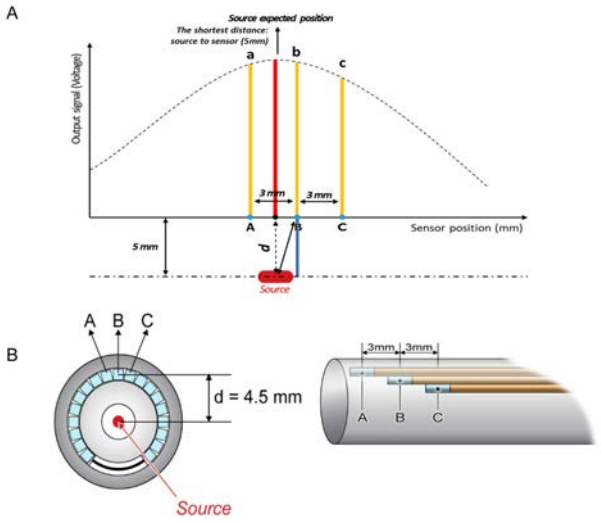


**FIGURE 4.** Diagram of the inverse square function fitting method: A. diagram of the correlation between the expected source position and the output signals of the sensors, B. The layout of the array of sensors and a source inside the applicator.

We also fitted the data based on the inverse-square law using Microsoft Excel. We calculated the expected position of the source using Eqs. (2) and (3). We fitted three output signal data from the sensor with the maximum output signal and two adjacent sensors to find the source position. We assumed that the source was adjacent to the sensor with the maximum output, as shown in Fig. 4. Moreover, we used the Euclidean distance between the source and the sensor position to obtain two quadratic equations (Eqs. (2) and (3)), which we utilized to predict the location of the source. Then, we calculated the Euclidean distance (r), which is the expected source position. The values of a, b, and c are the signal outputs of each sensor, and d is the vertical distance between the source and the sensor axis.

$$\frac{b}{a} = \frac{(3-r)^2 + d^2}{r^2 + d^2} \tag{2}$$

$$\frac{b}{c} = \frac{(3+r)^2 + d^2}{r^2 + d^2} \tag{3}$$

In the case where the dwell position was set so that the source moved in 10-mm increments, thin and 5-mm-width EBT3 film was inserted into the applicator of the SFRMS to determine the distance between the source dwell position and the sensors. We compared the distance between the planned and measured dwell positions using the sensor outputs and the EBT3 film. The output data used to analyze the peak position were collected during the irradiation of the EBT3 film.

### 3) DWELL TIME ACCURACY MEASUREMENT

To evaluate the accuracy of dwell-time monitoring, measurements were taken in a single position with the source dwell time set to 1, 2, 3, 6, 10, 20, 30, 40, 50, or 60 s. Our SFRMS's data sampling frequency is 1000 Hz and the one signal is counted every 0.001 sec and is accumulated as raw data.

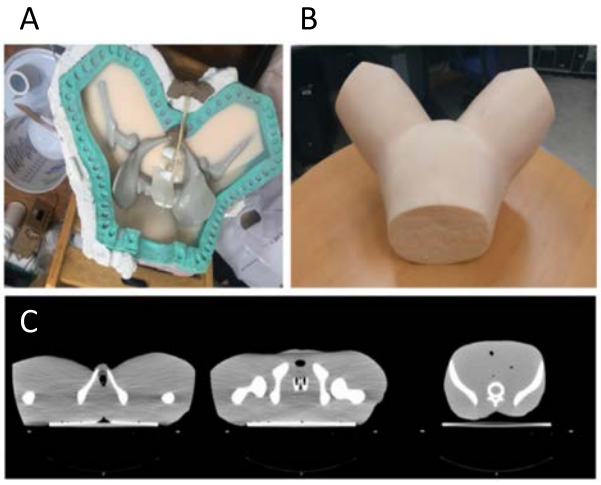


**FIGURE 5.** Silicon based human phantom: A. Inside, B. outside, C. CT images.

When the radiation source stops at the dwell position, the highest signal is provided from the sensor near the dwell position as shown in Fig. 2 B, and the sensors' signal far from the dwell position decreases as the shape of the step. Then count the number of signals measured until the signal output of the corresponding sensor decreases as the radiation source begins to move again. The dwell time is the measured number of signals multiplied by sampling time. For excluding the optical noise such as Cerenkov radiation and the background signal, we counted the signals at each measurement by using a threshold of 15% of the maximum output.

We checked the time at which the signal data were measured, based on the planned irradiation time and the data. And we compared the expected irradiation time with the identified time from the data to confirm the difference and evaluated the linearity of the data over time.

### 4) PHANTOM STUDY

A phantom study was conducted for two reasons. The first goal was to test the measurement accuracy of the SFRMS when the source moved as same as the treatment plan for an actual patient. And the second goal was to determine the correlation between the applicator's location and the DVH. For the phantom study, we performed computed tomography (CT) scanning of a silicon-based anthropomorphic phantom with the applicator inserted. The phantom used inserts with densities and geometries that mimicked the effects of human anatomy (Fig. 5). The silicone phantom was designed around the organs of the lower abdomen (e.g., pelvic bone, bladder, vagina, rectum, and anus).

To test the accuracy of the dwell position and dwell time, we evaluated the performance of the SFRMS using the patient treatment plan. We used two patient treatment plans to analyze the CT images and evaluated the differences in dwell positions and dwell times of the source between the plans and measurements. The Patient-1 plan included five treatment points, each with a different source dwell time.

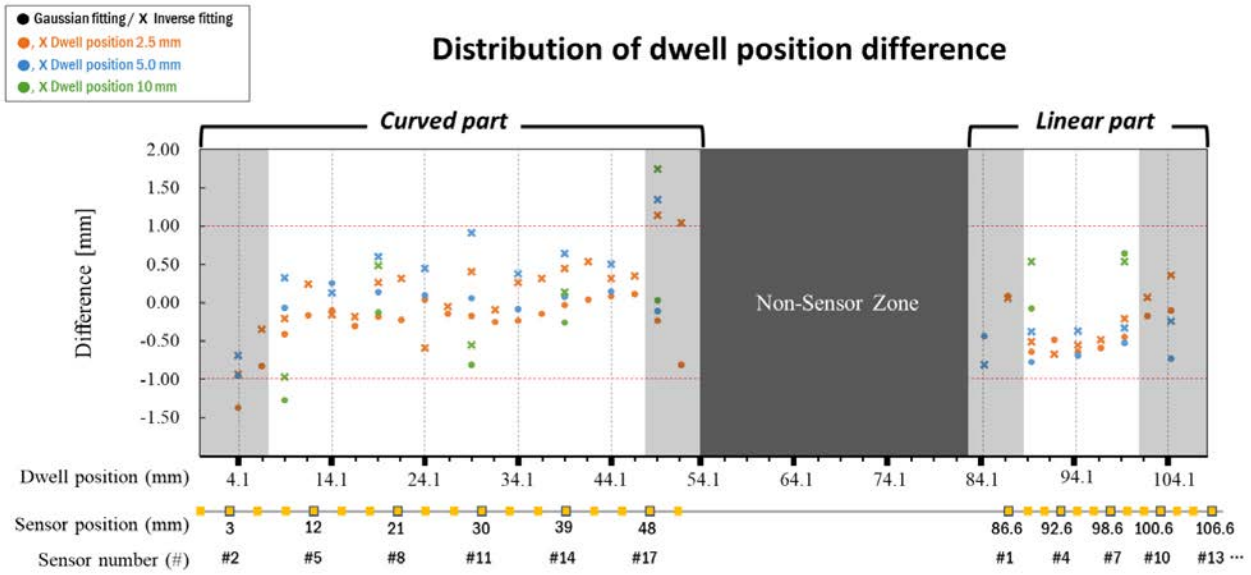


**FIGURE 6.** Distribution of the overall results compared at dwell positions 2.5, 5.0, and 10 mm: The average difference of dwell position for 2.5, 5.0, 10 mm. The sensor is positioned every 3 mm in curved part and 2 mm in linear part.

The five treatment points in the Patient-1 plan were 4.1, 14.1, 24.1, 34.1, and 44.1 mm from the tip of the catheter, with dwell times of 95.1, 65.6, 65.6, 65.6, and 17.2 s, respectively. The Patient-2 plan included three treatment points with dwell positions of 4.1, 9.1, and 34.1 mm from the tip of the catheter and dwell times of 71.3, 118.8, and 59.4 s, respectively.

To determine the correlation between the applicator's location and the DVH, a dose comparison was performed. After projecting the treatment plan onto the phantom and acquiring the applicator CT image with CT-Simulation, we determined how much the DVH differed from the actual patient treatment plan if the SFRMS location in the patient's body was shifted by 2.5 mm or 5.0 mm. Two important locations for HDR-BT were reported in 1953 [32]: Manchester prescription points A and B. Point A is the major critical point for brachytherapy dose specification and is located 2 cm above the external uterus and 2 cm lateral to the uterine tandem in the plane of the uterus. Point B represents the pelvic sidewall/obturator nodes and is located 5 cm lateral to the midline at the same level as point A. In these cases, the two patients were treated with 5.8 Gy $\times$ 5 fx (fraction), and the dose was normalized based on point A. The doses for Patient-1 at point A were prescribed as 10.11 Gy (left) and 9.856 Gy (right), and the doses at point B were 2.332 Gy (left) and 2.338 Gy (right).

## III. RESULTS

### A. DWELL POSITION ACCURACY

We compared the planned source position to the fitted data when moving the dwell position; the averages and standard deviations are shown in Table 1. The differences in the average and standard deviation between the planned source position and the position predicted with the Gaussian function were within $-0.63 \pm 0.13$ mm. Furthermore, for the position predicted by the inverse-square function, all differences were within $0.72 \pm 0.26$ mm. Fig. 6 shows the distribution of the overall results at dwell positions of 2.5, 5.0, and 10 mm. Most differences were within 1 mm. The error was relatively high when the dwell position was adjacent to the non-sensor area. The deviation from the planned source position was found to be as large as 1.45 mm.

**TABLE 1.** Dwell position accuracy check: Difference between the planned source position and fitting position (average data).

| Fitting Method | Gaussian (mean ± STDV, mm) | | Inverse Square (mean ± STDV, mm) | |
|---|---|---|---|---|
| Dwell position | Curved Part | Linear Part | Curved Part | Linear Part |
| 2.5 mm | -0.26 ± 0.35 | -0.37 ± 0.26 | 0.16 ± 0.48 | -0.24 ± 0.35 |
| 5.0 mm | -0.04 ± 0.32 | -0.63 ± 0.13 | 0.46 ± 0.50 | -0.40 ± 0.20 |
| 10 mm | -0.56 ± 0.45 | 0.28 ± 0.44 | -0.16 ± 0.95 | 0.72 ± 0.26 |

After moving the source position by 10 mm, we compared the expected source position with the photosensitive position on the EBT3 film. The errors are displayed in Table 2. Independent measurements were performed using the fiber-based real-time monitoring system and the EBT3 film. The average difference between the dwell position and the film at the curved part (dwell position 4.01–24.01 mm) was found to be $0.29 \pm 0.59$ mm. The average difference between the peak position based on the output and the film was found to be $0.04 \pm 0.15$ mm. The output data used for analyzing the peak position were acquired during the irradiation of the EBT3 film, and it was found that the measured data and the film results matched. Additionally, the difference between

**TABLE 2. Dwell position accuracy check: difference between the dwell position and output with EBT3 film.**

| Data [mm] | | | Difference [mm] | |
|---|---|---|---|---|
| Dwell Position | Peak position (Output) | EBT3 Film | Dwell position – Film | Peak position (Output) – Film |
| 4.010 | 4.671 | 4.541 | -0.53 | 0.13 |
| 14.01 | 13.34 | 13.18 | 0.83 | 0.16 |
| 24.01 | 23.27 | 23.44 | 0.57 | -0.17 |
| Mean ± STDV | | | 0.29 ± 0.59 | 0.04 ± 0.15 |

the dwell position and the output peak position was 0.25 ± 0.645 mm, which was similar to the results of the EBT3 error. The differences between the actual positions of the source (dwell position) and the peak positions predicted by the output were less than 1 mm (position 4.01 mm ①: −0.661 mm; position 14.01 mm ②: 0.67 mm; and position 24.01 mm ③: 0.74 mm).

### B. DWELL-TIME ACCURACY

We confirmed the linearity of the time difference and time counts. Table 3 shows that the difference between the dwell times set in the treatment planning system and the identified times based on data from the SFRMS were within 0.1 s. The signal counts (1028, 2054, 3055, 5026, 9999, 20035, 30045, 40000, 50034, 60072) generated by the scintillation fibers increased linearly with the increase of the set dwell times (1, 2, 3, 5, 10, 20, 30, 40, 50, and 60 s). We confirmed that the measured dwell times increased linearly as the set dwell time increased through a single polynomial fitting for the measured dwell times. For the 1-dimensional polynomial fitting, the p value was 0.9999 and the chi-square value was 0.003550.

**TABLE 3. Dwell time accuracy.**

| Dwell Time [s] | Measured Time [s] | Time Difference [s] |
|---|---|---|
| 1 | 1.028 | -0.028 |
| 2 | 2.054 | -0.054 |
| 3 | 3.055 | -0.055 |
| 5 | 5.026 | -0.026 |
| 10 | 9.999 | 0.001 |
| 20 | 20.035 | -0.035 |
| 30 | 30.045 | -0.045 |
| 40 | 40.000 | 0.000 |
| 50 | 50.034 | -0.034 |
| 60 | 60.072 | -0.072 |

### C. PHANTOM STUDY

We used silicon phantoms to validate the treatment plan for two patients receiving HDR-BT. The signal according to the patient treatment plan was confirmed via the real-time channel signal output from a LabVIEW-based monitoring system. The source dwell position was estimated using the Gaussian and inverse-square functions. The dwell position differences between the first and second treatment plans are shown in Table 4. The dwell time error was 0.76 ± 1.3 s for Patient-1 and 0.44 ± 0.40 s for Patient-2.

**TABLE 4. Phantom study: dwell position accuracy.**

| Patient Case | Patient 1 | | Patient 2 | |
|---|---|---|---|---|
| Fitting method | Gaussian | Inverse Square | Gaussian | Inverse Square |
| mean ± STDV [mm] | -0.88 ± 0.29 | -0.85 ± 0.36 | -0.53 ± 0.46 | -0.55 ± 0.30 |

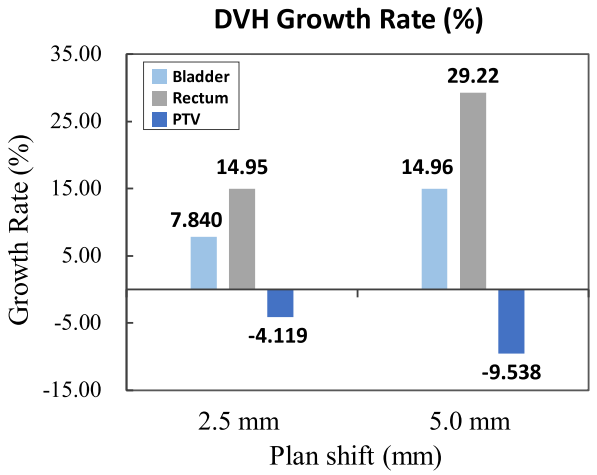


**FIGURE 7. Change in dose volume histogram (DVH) when the radioactive source shifted 2.5 and 5.0 mm: DVH changes in the bladder, rectum, and target of Patient-1.**

In this study, we evaluated the change in dose volume histogram (DVH) from the original Patient-1 plan (i.e., rectum, bladder, and planning target volume (PTV)) when the radioactive source shifted 2.5 and 5.0 mm in one direction (toward the back) (Fig. 7). $D_{2cc}$ was the minimum dose to the most irradiated 2 cc area of the rectum and bladder [33], with differences in $D_{2cc}$ caused by these shifts being less than 1%. However, in the case of the rectum, when compared to the original plan, the volume that received 60% of the dose increased by 14.95% for the 2.5-mm shift and by 29.22% for the 5.0-mm shift. In the case of the bladder, the volume that received 50% of the dose increased by 7.84% for the 2.5-mm shift and by 14.96% for the 5.0-mm shift. Fig. 5 shows that the DVH increased in the organs at risk and decreased in the PTV as the dwell position shifted from the original plan.

When the dwell position was shifted from the original plan, the doses at BT prescription points A and B were also reduced. When the source position was moved 2.5 mm in a uniform manner, the doses at point A decreased by 3.93% (left) and 3.25% (right), and those at point B decreased by 1.53% (left) and 1.111% (right) compared with those in the original plan. When the source position was moved 5.0-mm, the doses at point A decreased by 9.42% (left) and

7.842% (right), and those at point B decreased by 3.38% (left) and 2.53% (right).

## IV. DISCUSSION

We evaluated the feasibility of the homemade real-time monitoring system for HDR-BT. Specifically, we evaluated the accuracy of the dwell position and the dwell time measured by the SFRMS.

Compared with the 1-mm dwell position accuracy and 0.1 s dwell time accuracy of the TG-56, TG-59, and IAEA recommendations [10], [11], [34]–[37], our SFRMS dwell position and dwell time accuracy were found to be within 0.72 mm and 0.055 s. However, because of structural constraints, this study was limited by including the source movement uncertainty (±0.5 mm) related to the proximity of the radiotherapy device in the measurement [38]. The uncertainty in the measurement can be divided into two categories. The first part is the uncertainty of the dwell position and dwell time due to the HDR. The HDR afterloader used in this experiment is the microSelectron Digital afterloader of Nucletron and $^{192}$Ir. The uncertainty of the dwell position and dwell time of this equipment was ± 0.5 mm and 0.1 s, respectively. The second part is related to the SFRMS, including systematic uncertainty of the geometrical limits of the SFRMS and the measurement itself. Geometrical uncertainty is expected to cause an error (100 $\mu$m) when fabricating an applicator with a milling machine, and can also cause measurement errors (1.5 mm at most) from the sensor array with a length of 2 mm located at intervals of 2 and 3 mm.

In 2013, Wootton and Beddar [39] reported the temperature dependence of a BCF-12 scintillation fiber. They reported that the total intensity of the light generated by the BCF-12 decreased by 0.13% per Celsius degree (°C) increase. The SFRMS was not significantly affected by the temperature because this system does not rely on absolute dose measurements like the PSD mentioned above [19], [20]. The SFRMS measures relative outputs from multiple sensors spaced 2 or 3 mm apart. The PSD system predicts the dwell position based on the output measured by the PSD. However, the SFRMS calculates the peak position in the relative output distribution of each sensor. The spacing between the arranged sensors is a significant factor in determining the accuracy of the position measurement. Even if the temperature changes, the difference in the relative output is not expected to be significant because all the sensors in the system change similarly. In a worst-case scenario, even if the temperature difference between each sensor was greater than 10 °C, the difference in the signal would be approximately 1.3%, which is unlikely to have a significant impact on the SFRMS, which finds the dwell position using the relative signal difference.

Our SFRMS was limited because it could not measure the source position between the curved and linear parts of the non-sensor zone. The errors were high in the dwell position in front and behind the curved part and the dwell position in front and behind the linear part. Errors occurred at those specific locations as a result of a lack of data needed for analysis because of the lack of sensors. Fig. 6 shows the differences between the planned and measured dwell positions as a function of the dwell position and sensor position. This figure shows that the difference between the planned and measured dwell positions increases when the dwell position is near the non-sensor zone. When the data points of the sensors in the non-sensor area or adjacent to the non-sensor region were excluded from the reanalysis, the standard deviation of the dwell position difference was reduced (Table 5). Because the data exclusion left only one data point for the linear parts in the case of the 10-mm dwell position, only the 2.5- and 5.0-mm dwell positions, as well as a 10-mm segment of the curved part, were reanalyzed. The absolute average differences between the planned and measured dwell positions were 0.23 and 0.62 mm for the sensor and non-sensor adjacent regions, respectively. Finally, the deviations in the dwell position between the plans and estimated data were 0.25 mm for the Gaussian fitting and 0.39 mm for the inverse-square fitting. Additionally, the effect of the source shape was not considered; only the output value of each sensor for the distance between the center of the source and the sensor was considered in this study. Therefore, the results include additional uncertainties as a result of not considering the geometry of the source itself.

**TABLE 5. Data reanalysis (2.5 and 5.0 mm).**

| Fitting method | Gaussian fitting | | Inverse-square fitting | |
|---|---|---|---|---|
| | Curved Part | Linear part | Curved Part | Linear part |
| Dwell position 2.5 mm | | | | |
| All Data | -0.26±0.35 | -0.37±0.26 | 0.16±0.48 | -0.24±0.35 |
| Data Select | -0.17±0.21 | -0.49±0.16 | 0.17±0.38 | -0.39±0.25 |
| Dwell position 5.0 mm | | | | |
| All Data | -0.04±0.32 | -0.63±0.13 | 0.46±0.50 | -0.42±0.20 |
| Data Select | 0.08±0.11 | -0.66±0.10 | 0.49±0.22 | -0.36±0.02 |
| Dwell position 10 mm | | | | |
| All Data | -0.56±0.45 | 0.28±0.44 | 0.16±0.95 | 0.72±0.26 |
| Data Select | -0.39±0.29 | - | 0.03±0.43 | - |

Incorrect movements of the radiation source can result in the target receiving a dose is considerably different from the planned dose. This may lead to an unintentional overdose to normal organs, such as the bladder and rectum. Our proposed monitoring system can verify the correctness of the treatment through real-time verification of the dwell position.

## V. CONCLUSION

Our study demonstrated the feasibility of a homemade scintillation fiber-based real-time monitoring system for High-dose-rate brachytherapy. We confirmed that the proposed SFRMS met the accuracy criteria of international guidelines;

Dwell position accuracy 0.72 mm, Dwell time accuracy 0.055 sec. Our system is valuable for use as a quality assurance device for pre-treatment patient specific plan verification or routine machine check. However, the current system has difficulty determining the in vivo dosimetry exactly because the system does not provide the exact dose measurement and the applicator is thick (∼2 cm diameter), thereby making it difficult to insert the applicator into the patient's body in clinical settings. The current version has a non-sensor zone between the curved and linear parts. In future work, we will develop thinner scintillation fibers (0.25 mm) to minimize interference with dose delivery.

## ACKNOWLEDGMENT

*(Jinsung Kim is co-first author.) (Sang Hyoun Choi contributed equally to this work.)* The authors would like to thank Medical Illustration & Design, a part of the Medical Research Support Services of the Yonsei University College of Medicine, for all artistic support related to this work.

## REFERENCES

[1] P. M. Devlin, *Brachytherapy: Applications and Techniques*. New York, NY, USA: Springer, 2015.

[2] M. Bethesda, "ICRU report 38. Dose and volume specification for reporting intracavitary therapy in gynecology," Int. Commission Radiat. Units Meas., Bethesda, MA, USA, Tech. Rep. 38, 1985, pp. 1–20.

[3] H. Yamazaki, K. Masui, G. Suzuki, S. Nakamura, D. Shimizu, T. Nishikawa, H. Okabe, K. Yoshida, T. Kotsuma, E. Tanaka, K. Otani, Y. Yoshioka, and K. Ogawa, "High-dose-rate brachytherapy monotherapy versus image-guided intensity-modulated radiotherapy with helical tomotherapy for patients with localized prostate cancer," *Cancers*, vol. 10, no. 9, p. 322, Sep. 2018, doi: 10.3390/cancers10090322.

[4] M. Uyeda, F. Friedrich, and A. C. A. Pellizzon, "High dose rate (HDR) brachytherapy in gynecologic cancer regression: A review of the literature," *Appl. Cancer Res.*, vol. 38, no. 1, pp. 1–8, Dec. 2018, doi: 10.1186/s41241-018-0070-z.

[5] B. W. Fischer-Valuck, H. A. Gay, S. Patel, B. C. Baumann, and J. M. Michalski, "A brief review of low-dose rate (LDR) and high-dose rate (HDR) brachytherapy boost for high-risk prostate," *Frontiers Oncol.*, vol. 9, p. 1378, Dec. 2019, doi: 10.3389/fonc.2019.01378.

[6] L. C. Mendez and G. C. Morton, "High dose-rate brachytherapy in the treatment of prostate cancer," *Transl. Androl. Urol.*, vol. 7, no. 3, pp. 357–370, Jun. 2018, doi: 10.21037/tau.2017.12.08.

[7] C. H. Wu, Y. J. Liao, Y. W. Liu, S. K. Hung, M. S. Lee, and S. M. Hsu, "Dose distributions of an $^{192}$Ir brachytherapy source in different media," *BioMed Res. Int.*, vol. 2014, Jan. 2014, Art. no. 946213, doi: 10.1155/2014/946213.

[8] S. Y. Moon, E. Jeong, Y. K. Lim, W. K. Chung, H. D. Huh, D. W. Kim, and M. Yoon, "Feasibility study of source position verification in HDR brachytherapy using scintillating fiber," *Prog. Med. Phys.*, vol. 27, no. 4, p. 213, 2016, doi: 10.14316/pmp.2016.27.4.213.

[9] H. M. L. Rosales, P. Duguay-Drouin, L. Archambault, S. Beddar, and L. Beaulieu, "Optimization of a multipoint plastic scintillator dosimeter for high dose rate brachytherapy," *Med. Phys.*, vol. 46, no. 5, pp. 2412–2421, May 2019, doi: 10.1002/mp.13498.

[10] V. Aguilar *et al.*, "Design and implementation of a radiotherapy programme: Clinical, medical physics, radiation protection and safety aspects," Int. At. Energy Agency, Vienna, Austria, Tech. Note 1040, 1998.

[11] H. D. Kubo, G. P. Glasgow, T. D. Pethel, B. R. Thomadsen, and J. F. Williamson, "High dose-rate brachytherapy treatment delivery: Report of the AAPM radiation therapy committee task group no. 59," *Med. Phys.*, vol. 25, no. 4, pp. 375–403, Apr. 1998, doi: 10.1118/1.598232.

[12] S.-Y. Park, J. M. Park, J.-I. Kim, S. Lee, and C. H. Choi, "Validation of new transmission detector transmission factors for online dosimetry: An experimental study," *Radiat. Oncol.*, vol. 13, no. 1, pp. 1–9, Dec. 2018.

[13] G. Razinskas, S. Wegener, J. Greber, and O. A. Sauer, "Sensitivity of the IQM transmission detector to errors of VMAT plans," *Med. Phys.*, vol. 45, no. 12, pp. 5622–5630, Dec. 2018.

[14] P. Doolan, M. Nikolaou, K. Ferentinos, and G. Anagnostopoulos, "Assessment of a commercial EPID dosimetry system to detect radiotherapy treatment errors," *Biomed. Phys. Eng. Exp.*, vol. 7, no. 4, Jul. 2021, Art. no. 047001.

[15] R. L. Smith, M. L. Taylor, L. N. McDermott, A. Haworth, J. L. Millar, and R. D. Franich, "Source position verification and dosimetry in HDR brachytherapy using an EPID," *Med. Phys.*, vol. 40, no. 11, Nov. 2013, Art. no. 111706, doi: 10.1118/1.4823758.

[16] E. H. Jeang, Y. Goh, K. H. Cho, S. Min, S. H. Choi, H. Jeong, K. Jo, N. Lee, S. Song, S. B. Lee, D. Shin, Y.-J. Kim, J.-Y. Kim, D. Y. Kim, U.-J. Hwang, and Y. K. Lim, "Two-dimensional *in vivo* rectal dosimetry during high-dose-rate brachytherapy for cervical cancer: A phantom study," *Acta Oncologica*, vol. 57, no. 10, pp. 1359–1366, Oct. 2018, doi: 10.1080/0284186X.2018.1484155.

[17] P. Casolaro, L. Campajola, G. Breglio, S. Buontempo, M. Consales, A. Cusano, A. Cutolo, F. Di Capua, F. Fienga, and P. Vaiano, "Real-time dosimetry with radiochromic films," *Sci. Rep.*, vol. 9, no. 1, p. 5307, Mar. 2019, doi: 10.1038/s41598-019-41705-0.

[18] Z.-Y. Qi, X.-W. Deng, S.-M. Huang, J. Lu, M. Lerch, D. Cutajar, and A. Rosenfeld, "Verification of the plan dosimetry for high dose rate brachytherapy using metal-oxide-semiconductor field effect transistor detectors," *Med. Phys.*, vol. 34, no. 6, pp. 2007–2013, May 2007, doi: 10.1118/1.2736288.

[19] F. Therriault-Proulx, T. M. Briere, F. Mourtada, S. Aubin, S. Beddar, and L. Beaulieu, "A phantom study of an *in vivo* dosimetry system using plastic scintillation detectors for real-time verification of $^{192}$Ir HDR brachytherapy," *Med. Phys.*, vol. 38, no. 5, pp. 2542–2551, May 2011, doi: 10.1118/1.3572229.

[20] S. B. C. Debnath, M. Ferre, D. Tonneau, C. Fauquet, A. Tallet, A. Goncalves, and J. Darreon, "High resolution small-scale inorganic scintillator detector: HDR brachytherapy application," *Med. Phys.*, vol. 48, no. 4, pp. 1485–1496, Apr. 2021.

[21] J. G. Johansen, S. Rylander, S. Buus, L. Bentzen, S. B. Hokland, C. S. Søndergaard, A. K. M. With, G. Kertzscher, and K. Tanderup, "Time-resolved *in vivo* dosimetry for source tracking in brachytherapy," *Brachytherapy*, vol. 17, no. 1, pp. 122–132, Jan. 2018, doi: 10.1016/j.brachy.2017.08.009.

[22] E. B. Jørgensen, G. Kertzscher, S. Buus, L. Bentzen, S. B. Hokland, S. Rylander, K. Tanderup, and J. G. Johansen, "Accuracy of an *in vivo* dosimetry-based source tracking method for afterloading brachytherapy—A phantom study," *Med. Phys.*, vol. 48, no. 5, pp. 2614–2623, May 2021, doi: 10.1002/mp.14812.

[23] J. Mason, A. Mamo, B. Al-Qaisieh, A. M. Henry, and P. Bownes, "Real-time *in vivo* dosimetry in high dose rate prostate brachytherapy," *Radiotherapy Oncol.*, vol. 120, no. 2, pp. 333–338, Aug. 2016.

[24] G. Kertzscher, A. Rosenfeld, S. Beddar, K. Tanderup, and J. Cygler, "*In vivo* dosimetry: Trends and prospects for brachytherapy," *Brit. J. Radiol.*, vol. 87, no. 1041, 2014, Art. no. 20140206.

[25] F. Verhaegen, G. P. Fonseca, J. G. Johansen, L. Beaulieu, S. Beddar, P. Greer, N. Jornet, G. Kertzscher, B. McCurdy, R. L. Smith, B. Mijnheer, I. Olaciregui-Ruiz, and K. Tanderup, "Future directions of *in vivo* dosimetry for external beam radiotherapy and brachytherapy," *Phys. Imag. Radiat. Oncol.*, vol. 16, pp. 18–19, Oct. 2020.

[26] G. P. Fonseca, J. G. Johansen, R. L. Smith, L. Beaulieu, S. Beddar, G. Kertzscher, F. Verhaegen, and K. Tanderup, "*In vivo* dosimetry in brachytherapy: Requirements and future directions for research, development, and clinical practice," *Phys. Imag. Radiat. Oncol.*, vol. 16, pp. 1–11, Oct. 2020.

[27] *Organic Scintillation Materials and Assemblies*, Saint-Gobain Ceram. Plastics, Malvern, PA, USA, 2021. [Online]. Available: https://www.crystals.saint-gobain.com/sites/sites/hps-mac3-cma-crystals/files/2021-12/Organics-Plastic-Scintillators.pdf

[28] D. L. Chichester, S. M. Watson, and J. T. Johnson, "Comparison of BCF-10, BCF-12, and BCF-20 scintillating fibers for use in a 1-dimensional linear sensor," *IEEE Trans. Nucl. Sci.*, vol. 60, no. 5, pp. 4015–4021, Oct. 2013, doi: 10.1109/TNS.2013.2277799.

[29] C. Whittaker, C. A. Kalnins, D. Ottaway, N. A. Spooner, and H. Ebendorff-Heidepriem, "Transmission loss measurements of plastic scintillating optical fibres," *Opt. Mater. Exp.*, vol. 9, no. 1, pp. 1–12, 2019.

[30] L. Ding, Q. Wu, Q. Wang, Y. Li, R. M. Perks, and L. Zhao, "Advances on inorganic scintillator-based optic fiber dosimeters," *EJNMMI Phys.*, vol. 7, no. 1, p. 60, Dec. 2020.
[31] J. Lambert, Y. Yin, D. McKenzie, S. Law, and N. Suchowerska, "Cerenkov light spectrum in an optical fiber exposed to a photon or electron radiation therapy beam," *Appl. Opt.*, vol. 48, no. 18, pp. 3362–3367, 2009.
[32] M. Tod and W. Meredith, "Treatment of cancer of the cervix uteri—A revised 'Manchester method,'" *Brit. J. Radiol.*, vol. 26, no. 305, pp. 252–257, 1953.
[33] K. D. Romano, C. Hill, D. M. Trifiletti, M. S. Peach, B. J. Horton, N. Shah, D. Campbell, B. Libby, and T. N. Showalter, "High dose-rate tandem and ovoid brachytherapy in cervical cancer: Dosimetric predictors of adverse events," *Radiat. Oncol.*, vol. 13, no. 1, p. 129, Dec. 2018, doi: 10.1186/s13014-018-1074-2.
[34] R. Nath, L. L. Anderson, J. A. Meli, A. J. Olch, J. A. Stitt, and J. F. Williamson, "Code of practice for brachytherapy physics: Report of the AAPM radiation therapy committee task group no. 56," *Med. Phys.*, vol. 24, no. 10, pp. 1557–1598, Oct. 1997, doi: 10.1118/1.597966.
[35] J. Steenhuizen, M. Harbers, A. Hoffmann, A. D. Leeuw, A. Rijnders, and M. Unipan, "NCS report 30: Code of practice for quality assurance of brachytherapy with Ir-192 afterloaders," Netherlands Commission Radiat. Dosimetry, Delft, The Netherlands, Tech. Rep. 30, 2018.
[36] N. Frenière, "COMP report: CPQR technical quality control guidelines for brachytherapy remote afterloaders," *J. Appl. Clin. Med. Phys.*, vol. 19, no. 2, pp. 39–43, Mar. 2018, doi: 10.1002/acm2.12272.
[37] *Regulations (NRC, 10 CFR) PART 35 Medocal use of Byproduct Material*, Nucl. Regulatory Commission, Washington, DC, USA, Nov. 2020. Accessed: May 10, 2021. [Online]. Available: https://www.nrc.gov/reading-rm/doc-collections/cfr/part035/full-text.html
[38] *MicroSelectron HDR Product Datasheet*, ELEKTA, Stockholm, Sweden, 2017.
[39] L. Wootton and S. Beddar, "Temperature dependence of BCF plastic scintillation detectors," *Phys. Med. Biol.*, vol. 58, no. 9, p. 2955, 2013.

**NA HYE KWON** received the B.S. degree in radiology from the Catholic University of Pusan, Busan, South Korea, in 2017, and the M.S. degree in nuclear engineering from Kyung Hee University, Yongin, South Korea, in 2020. She is currently pursuing the Ph.D. degree in medicine with Yonsei University, Seoul, South Korea.

From April to July 2017, she was an Intern with the Korea Institute of Nuclear Safety (KINS), Daejeon, South Korea. From August 2019 to September 2020, she was a Researcher with Kyung Hee University Hospital at Gangdong, Seoul. She is the author of four articles. Her research interests include silicon carbide-based radiation detection, risk management of radiation oncology departments, and real-time dosimetry for radiation therapy beams and spectroscopy.

Dr. Kwon received the Excellent Oral Presentation Award from the Korean Society of Medical Physics, in 2019, and an Applied Radiation Science Award (Poster) at the Nuclear Analytical Techniques (NAT) Conference, in 2020.

**JINSUNG KIM** received the B.S., M.S., and Ph.D. degrees in nuclear and quantum engineering from the University of KAIST (Korea Advanced Institute of Science and Technology), Daejeon, in 2007.

From 2007 to 2008, he was a Postdoctoral Fellow, from 2008 to 2009, he was a Resident Medical Physicist with the National Cancer Center, Goyang, South Korea. From 2009 to 2016, he was a Clinical Assistant Professor with Samsung Hospital, Sungkyunkwan University, Seoul, South Korea, where he was a Research Assistant Professor with Samsung Hospital, from 2010 to 2016. From 2016 to September 2019, he was an Assistant Professor with the Radiation Oncology Department, Yonsei Cancer Center, Seoul. Since 2019, he has been an Associate Professor with the Radiation Oncology Department, Yonsei Cancer Center. He is the author of more than 107 articles. He holds seven patents. His research interests include medical artificial intelligence, auto-segmentation, advanced CT reconstruction, and proton/carbon ion therapy.

**JU HYE KIM** received the B.S. degree in radiological science from Yonsei University (Mirae Campus), Wonju, South Korea, in 2011, and the M.S. degree in medical science from Ewha Womans University, Seoul, South Korea, in 2015.

From 2015 to 2017, she was a Medical Physicist with the Yonsei Cancer Center, Seoul. From 2017 to 2018, she was a Researcher with Kyung Hee University Hospital at Gangdong, Seoul. From 2019 to 2020, she was a Medical Physicist with the CHA Bundang Medical Center, Sungnam, South Korea. Since 2021, she has been a Medical Physicist with the Radiation Oncology Department, Samsung Medical Center, Seoul. She is the author of nine articles and two technical reports. Her research interests include risk management of n radiation oncology departments, and real-time dosimetry.

Prof. Kim received the Excellent Oral Presentation Award from the Korean Society of Medical Physics, in 2012, and Poster Award from the Korean Society of Medical Physics, in 2015.

**SANG HYOUN CHOI** received the B.S., M.S., and Ph.D. degrees in nuclear engineering from Hanyang University, Seoul, South Korea, in 2005, 2007, and 2014, respectively.

From 2007 to 2013, he was a Medical Physicist with Inha University Hospital, Incheon, South Korea. From 2013 to 2014, he was a Senior Researcher with the Heavy Particle Safety Management Team, Korea Institute of Radiological Medical Sciences (KIRAMS), Seoul. Since 2014, he has been a Senior Researcher with the Research Team at Radiological Physics and Engineering, KIRAMS, Seoul, where he has been the Chief Technical Manager with the IAEA/WHO Secondary Standard Dosimetry Laboratory and IAEA DAN (Dosimetry Audit Networks), since 2017. He is the author of three books, more than 20 articles, and more than six inventions with patents. His research interests include silicon carbide detection for radiation measurement, micro dosimetry, radio activation using linac, and proton therapy.

**DONG WOOK KIM** (Member, IEEE) received the B.S. degree in physics and the M.S. degree in experimental high-energy physics from Gangneung National University, Gangneung, South Korea, in 1992 and 1994, respectively, and the Ph.D. degree in experimental particle physics from Sungkyunkwan University, Suwon, South Korea, in 2002.

From 2002 to 2006, he was a Research Fellow with Johns Hopkins University, Baltimore, MD, USA. From 2006 to 2007, he was a Senior Researcher with Seoul National University, Seoul, South Korea. From 2007 to 2010, he was a Medical Physics Fellow with the National Cancer Center, Goyang, South Korea. From 2010 to 2019, he was a Clinical Associate Professor with Kyunghee University Hospital at Gangdong, Seoul. Since 2019, he has been a Clinical Professor with the Radiation Oncology Department, Yonsei Cancer Center, Seoul. He is the author of five books, more than 160 articles, and more than 30 inventions with patents. His research interests include respiratory training for lung and liver patients, risk management of radiation oncology departments, real-time dosimetry for radiation therapy beams, and proton/carbon ion therapy.

Dr. Kim was a recipient of the Korean Society of Medical Physics Young Scientist Award for Excellence, in 2009. He has received two achievement Awards, as well the Korean Society of Medical Physics Excellent Research Paper Award, in 2020.